

Research Article

Enhanced Photocatalytic Activity of Hierarchical Macro-Mesoporous Anatase by ZrO₂ Incorporation

M. L. García-Benjume,¹ M. I. Espitia-Cabrera,² and M. E. Contreras-García¹

¹ Instituto de Investigaciones Metalúrgicas, Universidad Michoacana de San Nicolás de Hidalgo, Edificio "U" Ciudad Universitaria, 58060 Morelia, MICH, Mexico

² Facultad de Ingeniería Química, Universidad Michoacana de San Nicolás de Hidalgo, Edificio "U" Ciudad Universitaria, 58060 Morelia, MICH, Mexico

Correspondence should be addressed to M. E. Contreras-García, eucontre@zeus.umich.mx

Received 27 January 2012; Revised 12 March 2012; Accepted 13 March 2012

Academic Editor: Stéphane Jobic

Copyright © 2012 M. L. García-Benjume et al. This is an open access article distributed under the Creative Commons Attribution License, which permits unrestricted use, distribution, and reproduction in any medium, provided the original work is properly cited.

The effect of the addition of zirconia in the photocatalytic behaviour of titania is analysed. In order to increase the ways for reagent and product diffusion in the material, a sol-gel hydrothermal synthesis route using Tween-20 as a directing agent to obtain a hierarchical macro-mesoporous structure is proposed. Nanostructured macro-mesoporous TiO₂/ZrO₂ photocatalyst with 0, 10, 20, 30, and 100% mol of ZrO₂ were obtained and calcined at different temperatures. The crystalline structure was analyzed by X-ray diffraction and TEM. The porosity was confirmed by SEM, TEM, and nitrogen adsorption-desorption isotherms. The worm-like mesoporous structure was confirmed by TEM. The specific surface areas obtained by Brunauer-Emmet-Teller method (BET) ranged from 125 to 180 m²/g. The Tween-20 total elimination from the structure by thermal treatment was confirmed by infrared spectroscopy and thermogravimetric analysis. Additionally, the photocatalytic effect of the zirconia addition was studied in the methylene blue (MB) degradation reaction, and the best photocatalytic activity was obtained in the sample with 10% mol of ZrO₂, degrading up to 92% the MB.

1. Introduction

Recently, TiO₂ has been widely used for the preparation of different types of nanomaterials, including nanoparticles with different shapes (nanorods, nanowires, nanotubes, and nanoflowers) and also mesoporous and nanoporous TiO₂-containing materials [1]. Regardless of scale, TiO₂ maintains its photocatalytic abilities [2]. Nevertheless, TiO₂ can present low photocatalytic activity mainly due to the high electron-hole pair recombination rate and the fact that it can be only excited under UV light wavelength. In order to solve these problems, titania is combined with other oxides to form nanoconjugates in order to increase the energetic range at which the nanoparticles can be excited (photoresponse). This allows the TiO₂ nanoconjugates to be excited by energies in the visible light spectrum and to increase the ability of a photocatalytic material to overcome charge recombination and allow separated charges to interact with molecules at

the surface of the material (photocatalytic efficiency)[3–5]. The use of different nanoconjugates has been proposed to circumvent the partial photocatalytic reactivity of TiO₂ due to charge recombination and to increase the photoresponse of TiO₂, allowing nanoconjugates to be used for sterilization with sunlight in a most energy-effective way. Multiple additions can be made to TiO₂ nanoparticles to create TiO₂ nanoconjugates; these additions include noble metal deposition, doping with metal (Fe³⁺, Cu²⁺, Cr³⁺) and nonmetal ions (C, N, S, F) [6, 7], compositing with a polymer and the creation of core-shell magnetic nanoparticles. Currently, TiO₂ nanoconjugates are used in multiple antimicrobial, antifungal, and waste decontamination applications [8], and can also be used to sterilize medical devices such as catheters and dental implants [9, 10]. TiO₂ nanoconjugates have also been tested for the sterilization of food packaging and food preparation surfaces to prevent the bacterial contamination of food [11–13]. However, the most often used application

of TiO_2 nanoconjugates in this area has been for the purification of drinking water and decontamination of waste water [8, 14].

The semiconductors (CdS , ZnO , WO_3) [15] and other metal oxides ZnO , MnO_2 , Al_2O_3 [16, 17], ZrO_2 [18–20], Ta_2O_5 [21], and In_2O_3 when coupled to TiO_2 nanoparticles have also been shown as efficient in increasing the photocatalytic capability of TiO_2 nanoparticles [22–25]. The addition of MnO_2 or Al_2O_3 (charge-transfer catalysts) to TiO_2 nanoparticles broadens the excitation spectrum of TiO_2 to visible light ranges, as demonstrated by methylene blue degradation [22] and *E. coli* destruction [25].

$\text{ZrO}_2\text{-TiO}_2$ system has been the object of few studies, and ZrO_2 and TiO_2 have similar catalytic behaviors presenting amphoteric properties, which allows them to behave as either a Lewis acid or a Lewis base, depending on the pH of the solution used to wash the TiO_2 or ZrO_2 material [26].

Acidic conditions cause the TiO_2 to be positively charged and to exhibit anion-exchange properties [27]. Consequently, samples prepared for analysis on TiO_2 or ZrO_2 columns are often dissolved in an acidic solution so as to promote electrostatic binding between the positively and negatively charged groups [28] after which they can be desorbed under alkaline conditions [29].

Concerning the photocatalytic behavior of TiO_2 and ZrO_2 semiconductors, the TiO_2 band gap is 3.2 eV [30, 31] and the ZrO_2 is 3.4 [32]. The similar band gap of both oxides indicates a similar photocatalytic behavior. Nevertheless, the use of $\text{TiO}_2\text{-ZrO}_2$ nanoconjugates allows the creation of additional levels between TiO_2 's valence and conduction bands which act as traps that retard the surface migration of the electron-hole pairs leading to a reactive migration to the surface and the corresponding desorption of the oxidized or reduced species. An additional advantage in the use of ZrO_2 is that the zirconium stabilizes the anatase phase allowing its obtention at lower temperatures (<600°C) [33]. An additional point is that nanosized materials have high surface area to volume ratios, which allows them to bind to a much greater number of targets [2].

Otherwise, the macro-mesoporous structure proposed in this work for the $\text{TiO}_2\text{-ZrO}_2$ nanoconjugates enhances the catalytic efficiency due to the better transport of reactants and products through the hierarchical porous structure and also allows better light penetration into the photocatalytic material [34]. Zhang and Yu [30] have shown that the presence of extralarge meso-macroporous channels in the materials represent an efficient way for the reactants molecular species to reach the active sites on the porous walls.

In this paper, we demonstrate a self-formation phenomenon of hierarchy with multiple-scaled porosity, using Tween-20 as the structure direction agent in the photocatalytic system $\text{TiO}_2\text{-ZrO}_2$. Macrochanneled structures are formed, with openings ranging from 0.2 to 5 microns and wormhole-like mesoporous walls, with various $\text{TiO}_2\text{-ZrO}_2$ ceramic compositions that can be prepared just by controlling the hydrolysis and polycondensation conditions such as pH and using hydrothermal treatment. The macrochannels (funnel-like or straight) are parallel to each other and perpendicular to the tangent of the particles' surface.

These hierarchical porous ceramics can be used in catalysis, photocatalysis, separation and for the immobilization of biological molecules, and even microorganisms, for filtration and bioreactor applications [1].

2. Experimental Procedure

Two solutions were prepared, one of them was with surfactant (Tween-20 Fluka) water in weight ratio of 1:10 and the other was a butanol alcoholic solution of $\text{Ti}(\text{OC}_4\text{H}_9)_4$ and $\text{Zr}(\text{OC}_4\text{H}_9)_4$ (both from Sigma-Aldrich) in the stoichiometric ratios of 0, 10, 20, 30, and 100% mole of ZrO_2 . This solution was aggregated to the surfactant-water solution and was vigorously stirred. The sol obtained was hydrothermally processed at 80°C for 24 hours, dried at 100°C. Those samples were labeled as T, T10Z, T20Z, T30Z, and Z, respectively, and then calcined at 400°C for 3 hours at a heating rate of 1°C/min, after calcinations, the samples were labeled as T-400, T10Z-400, T20Z-400, T30Z-400, and Z-400, respectively. The sample T10Z was also calcined at 500°C for 3 hours at a heating rate of 1°C/min, this sample was labeled as T10Z-500.

In order to determine the suitable thermal treatment to totally eliminate the organic compounds, thermal analysis was carried out using a thermogravimetric (TG) analyzer, a Perkin Elmer Pyris Diamond model equipped with "Extar V6.2" software. The fresh samples were heated from room temperature to 400°C at a rate of 1°C/minute in air to determine the surfactant pyrolysis temperature. To corroborate the successful elimination of organics, Fourier transform infrared spectroscopy (FTIR) characterization was carried out on pellets of the calcined powders mixed with KBr (spectroscopy grade) and was recorded on a Bruker Tensor 27 spectrometer, in the range from 4000 to 400 cm^{-1} , at room temperature. The crystalline phases of the calcined powders were determined by X-ray diffraction (XRD) in a Philips X'PERT model diffractometer, using $\text{Cu K}\alpha$ radiation $\lambda = 1.54 \text{ \AA}$, with 0.02°/seg steps. A scanning electron microscope (SEM), JEOL JSM-6400 model, was used to observe the powder morphology. The nanoporous structure was observed by transmission electron microscopy (TEM) in a field emission FEI TECHNAI 200 microscope. The powder samples were dispersed in isopropyl alcohol and subject to ultrasonic treatment for five minutes, then they were deposited on a hole copper grid covered with an amorphous carbon film, by capillary deposition.

The powder samples were degassed at 200°C to obtain nitrogen adsorption-desorption isotherms, using Micrometrics ASAP 2010 Model equipment. The Brunauer-Emmet-Teller (BET) surface areas of the powder samples were calculated from the obtained isotherms. The pore size distributions were determined by the Barrett-Joyner-Halenda (BJH) method. The photocatalytic tests were carried out for methylene blue (MB) degradation using the obtained powders and TiO_2 P-25 Degussa powder as a reference, in a batch reactor consisting of a reaction cell with a compressed air supply in a tightly closed compartment equipped with an ultraviolet light using a Ultravg l25 6286 model lamp.

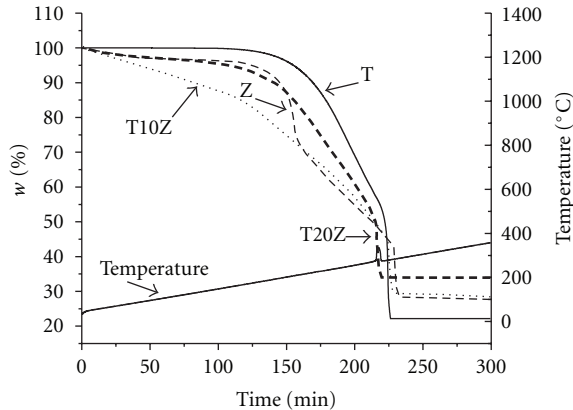


FIGURE 1: Thermograms of the $\text{TiO}_2\text{-}\text{ZrO}_2$ mixed oxides system (T10Z-400, T20Z-400, and Z-400 samples).

The reaction was carried out at room temperature in an aqueous solution with 10 mg/L of MB. The powder rate was one gram of oxides powder per litre of MB at pH = 7. The solution had been previously magnetically stirred at 400 rpm for 30 minutes without the use of UV light in order to reach a stable MB absorbance on the photocatalyst surface. Then, the solution was irradiated under UV light, magnetically stirred, and air was fed in simultaneously when the reaction system was started. Aliquots of powder sample suspensions were taken each hour during 5 h of testing. MB residual concentration was determined at 666 nm for absorbance using a Perkin-Elmer UV-Vis Lambda 20 spectrophotometer. Prior to the UV-Vis measurement, the suspensions were centrifuged at 2000 rpm by 5 minutes to eliminate the powder oxides interference during the test. The MB concentration after each experiment was determined quantitatively through the calibration graph constructed from standard solutions of MB at various concentrations.

3. Results and Discussion

3.1. Organic Compounds. Figure 1 presents the thermograms obtained for the mixed oxide system $\text{TiO}_2\text{-}\text{ZrO}_2$ (T10Z-400, T20Z-400, T-400, and Z-400 samples). In these thermograms, all samples continuously lost weight in a linear manner from 90°C until 300°C this weight loss corresponds to the adsorbed water and the butanol desorption [35–37]. Another form of weight loss, between 180 and 210°C, was present; this is because the alkoxides bonded strongly to the chemisorbed water. The pure zirconia sample, Z-400, presented a great weight loss, which leads to the conclusion that zirconia has less affinity than titania to these groups. Drastic weight loss was present from 270 to 300°C, which corresponds to surfactant and organic precursors pyrolysis [37, 38] all other weight loss was registered. These results confirm that surfactant has been removed completely at 400°C, this temperature is similar to the that previously reported by the authors for $\text{TiO}_2\text{-}\text{Al}_2\text{O}_3$ system [39].

Figure 2 shows the FT-IR spectra of T10Z-400, T20Z-400, T30Z-400, T-400, and Z-400 samples calcined at 400°C.

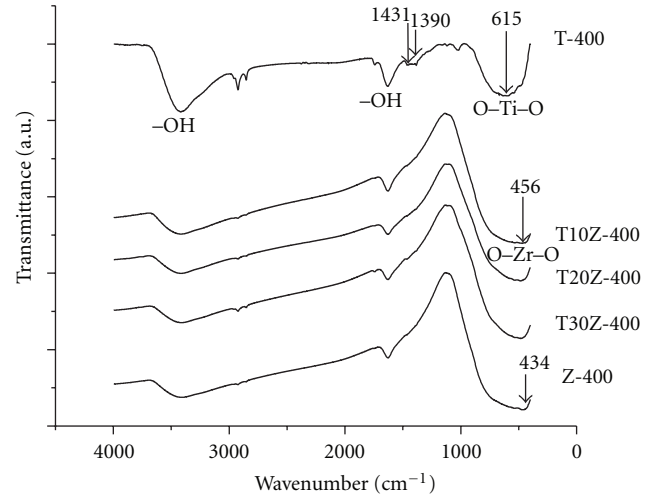


FIGURE 2: FT-IR spectra of T10Z-400, T20Z-400, T30Z-400, T-400, and Z-400 samples.

TABLE 1: Wave number of the main registered vibrations.

Frequency cm ⁻¹	Bond	Corresponds to
3411	O-H	Adsorbed water
1630	OH	Ti-OH, Zr-OH
2927, 1450		Tween-20 and organic precursors
2847, 1390	CH ₃ y CH ₂	
615	O-Ti-O	TiO ₂
456, 434	O-Zr-O	ZrO ₂

Table 1 presents the wave number of the registered vibrations. The O-Ti-O bonding vibration located at 615 cm⁻¹ is a broadband, the vibration at 1034 cm⁻¹ corresponds to the ester group present in Tween-20 [39], and this signal is not present in the mixed oxides or in ZrO₂ samples.

In the Z-400 sample, the bands at 456 and 434 cm⁻¹ are characteristic of Zr-O bond vibration of ZrO₂ in its tetragonal phase [40]; in the mixed oxides, those bands are low, displaced from 456 to 466 cm⁻¹. As the ZrO₂ content increases, the band presents better definition and is located at 456 cm⁻¹. The broadband characteristic of the O-Ti-O bond vibration, located at 615 cm⁻¹, does not allow differentiation of the characteristic bands in the mixed oxides systems. This behaviour is due to the fact, zirconium is the most electropositive transition metal and it presents a greater attraction to water [41] than to the organic part of Tween-20.

3.2. Crystalline Structure. The XRD results are presented in Figure 3(a). Sample T-400 only presents the anatase phase and Z-400 sample shows the tetragonal phase of zirconia ($t\text{-}\text{ZrO}_2$). Samples T10Z-400, T20Z-400, and T30Z-400 present both phases, anatase and $t\text{-}\text{ZrO}_2$. These results clearly show the composition effect in the principal peaks intensity. The tetragonal phase $t\text{-}\text{ZrO}_2$ is observed even at low concentration (10% mol de ZrO₂), so zirconia crystallization

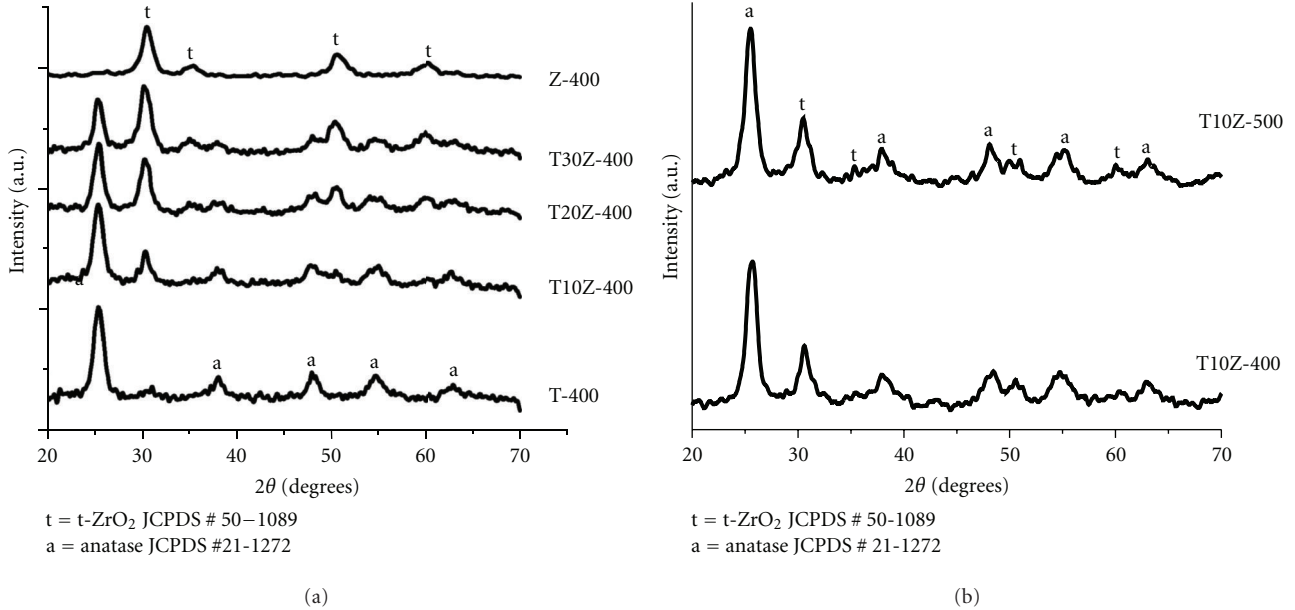


FIGURE 3: X-ray diffraction patterns (a) of T10Z-400, T20Z-400, T30Z-400, T-400, and Z-400 samples and (b) for sample T10Z calcined at 400 and 500°C.

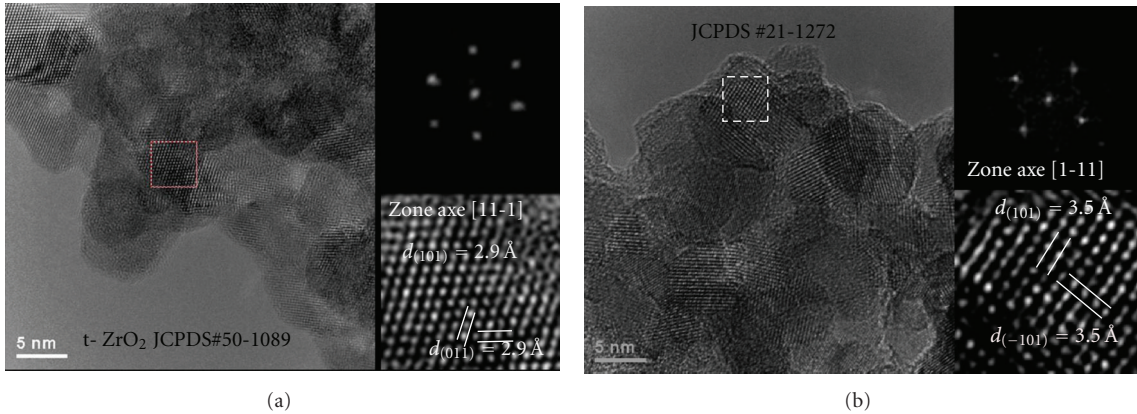


FIGURE 4: HRTEM images of T20Z-400 sample showing the nanoparticles forming the nanoconjugates, inserts present the FFT and the high-resolution indexed zone. (a) Zirconia nanocrystal indexed as tetragonal phase, (b) titania nanocrystal indexed as anatase phase.

was not affected by the presence of titania, and the anatase phase remains stable in the presence of zirconia. Figure 3(b) shows the XRD diffraction pattern for sample T10Z calcined at 400 and 500°C; from this result, it was found that anatase TiO₂ phase is thermally stable and the crystal size apparently is not affected when the sample was calcined between 400 and 500°C, because the full width at half maximum is (FWHM) very similar in both diffractograms.

High-resolution transmission electron microscopy (HRTEM) images of the T20Z-400 sample are shown in Figure 4. It is possible to distinguish nanoparticles with mean diameters between 7 and 11 nm. Figure 4(a) presents nanoparticles indexed as ZrO₂ in the tetragonal phase. Figure 4(b) presents a particle indexed at the anatase phase, in this image, the particles size diameters are between 4 to 12 nm.

3.3. Textural Properties. A SEM micrograph of the T10Z-400 sample, at low magnification (2000x) is presented in Figure 5(a). The morphology of this sample presents a smooth surface “skin-film” type formed by channels; the fracture surface of the particle allows us to observe the inside, showing a structure composed of spherical aggregates forming the porous walls. This complicated morphology can be observed better in Figure 5(b), which shows a micrograph at greater magnification (20000x). Figures 5(c) and 5(d) present SEM micrographs of the T20Z-400 sample, Figures 5(e) and 5(f) correspond to the T30Z-400 sample and Figures 5(g) and 5(h) correspond to the Z-400 sample.

Comparing these micrographs, it can be observed that the spherical aggregates size increases as the zirconia content is increased. In general, the macroporous structure is formed by channels, and the walls of these channels are formed by

agglomerated spherical particles, as a consequence of this the macroporous size increase too, as can be clearly seen in Figure 5(f). The pure zirconia Z-400 sample presents similar morphological characteristics.

The obtained macroporous structure will act as additional paths for light penetration into the oxide powders, helping to enhance the photocatalytic efficiency. The extinction of light in semiconductors follows the exponential law $I = I_0 \exp(-\alpha l)$, where I is the distance that light penetrates and α is the mutual penetration, which in titania has a value of $2.6 \times 10^4 \text{ cm}^{-1}$ at 320 nm. This implies, that at a wavelength of 320 nm, the light would be extinguished by 90% after having traversed a distance of 3900 Å or 390 nm of the photocatalytic material [42].

Figure 6(a) shows the TEM image obtained by the Z-contrast technique for sample T10Z-400. This image shows a porous zone around a sponge-like particle, this porous zone corresponding to macro-mesoporous textured powders.

Figure 6(b) presents thin and thick zones forming a sponge-like structure; in the thinnest zone, it is possible to distinguish the porosity in the sample, the dark zones are the mesoporous and the aggregates of different sizes. The bright particles have high zirconium concentration and the grey ones have high titanium concentration.

The mesoporous powder structure was observed by the TEM using an out-of-focus technique with underfocus and overfocus approaches, the resultant image can provide adequate contrast to be able to distinguish the channels [43]. This mesoporous structure can be seen in Figure 7 for the T20Z-400 sample, the image presents a “worm-like structure” [44], and this structure is typical for transition metals oxides where the bright and clear parts are the channels and the dark zones are the oxide walls. From this result, the porous diameters are from 2 to 4 nm.

The formation mechanism of the hierarchical macro-mesoporous structure of TiO_2 has been explained by different authors, Yu et al. [45] used the model proposed by Collins et al. [46] to explain the porous structure obtained with template-free photocatalytic hierarchical mesoporous TiO_2 . Collins has reported that the addition of surfactants could enhance the stability of microphase-separated interfaces, rather than serve as self-assembled templates. The mechanism has been also proposed for the porous structures obtained using Tween-20 as template for $\text{TiO}_2\text{-Al}_2\text{O}_3$ system in a previous work [39]. The similarity in the morphology obtained with and without template needs to be further investigated.

3.4. Macro-Mesoporosity. Figure 8(a) presents the adsorption-desorption N_2 isotherms for T-400, Z-400, T10Z-400, T20Z-400, and T30Z-400 samples. T-400 sample presents type IV isotherm characteristic for mesoporous materials which presents a hysteresis loop type H2 corresponding to pores with narrow necks and wider bodies [45, 47]. T10Z-400, T20Z-400, and T30Z-400 samples present type IV isotherms which present two hysteresis loops; this characteristic of the isotherm is associated to the bimodal pore size distributions in the mesoporous region [48]. The adsorption

TABLE 2: Specific surface areas and Pore mean diameters results.

Sample	Specific surface area (S_{BET}) m^2/g	Mean pore diameter (BJH adsorption) nm	Mean pore diameter (BJH desorption) nm
Z	45	16.2	15.7
T10Z-400	150	11	9
T10Z-500	182	4	3.8
T20Z-400	160	9.2	8
T30Z-400	128	10.4	9.1
T-400	136	8.5	6.6

curve at relative pressures between 0.6 and 0.8 presents a hysteresis loop type H2 corresponding to pores with narrow necks and wider bodies. At high relative pressures between 0.8 and 1, the shape of the hysteresis loop is type H3, associated with plate-like particles given rise to narrow slit shape porous. Sample Z-400 presents a isotherm with a combination of type III and IV; at relative pressures below 0.8, the isotherm corresponds to materials with low affinity for the adsorbate [49], in this case nitrogen, or otherwise due to the low specific surface area. At high relative pressures, the isotherm is type IV with hysteresis loop type H3.

Figure 8(b) presents the isotherms for T10Z-400 and T10Z-500 samples. T10Z-500 sample presents a type IV isotherm characteristic for mesoporous materials which present two hysteresis loops; this characteristic isotherm is associated to bimodal pore size distributions in the mesoporous region. At relative pressures between 0.3 and 0.7, the adsorption curve has the hysteresis loop type H2 corresponding to pores with narrow necks and wider bodies. At high relative pressures between 0.8 and 1, the shape of the hysteresis loop is type H3, associated with plate-like particles given rise to narrow slit porous shape. This characteristic isotherm is associated to the bimodal pore size distributions in the mesoporous. This is due to the presence of nanopores with sizes smaller than 5 nm and the correspondent high specific surface areas. Compared with the T10Z-400 sample isotherm, in the T10Z-500 sample isotherm, it can be observed the shifting to lower relative pressures this result indicates the best remotion of the organic compounds resulting in the increasing of the area and the decreasing of around 50% of the mesoporous size due to the pore walls contraction at higher temperature, which means that the interparticle porosity decreases the pore size [47].

Specific surface area results obtained by the N_2 absorption BET method for all samples are presented in Table 2. The specific surface areas increase when zirconia content is increased up to 20% mol content and diminish with further ZrO_2 content increase. In Figure 6, corresponding to 20% mol of ZrO_2 , the TEM image shows white and dense ZrO_2 aggregates according to EDS analysis not shown, this aggregates block out the mesoporous structure and it might be the reason of why the highest ZrO_2 concentrations of the lower specific surface areas are obtained. The highest value

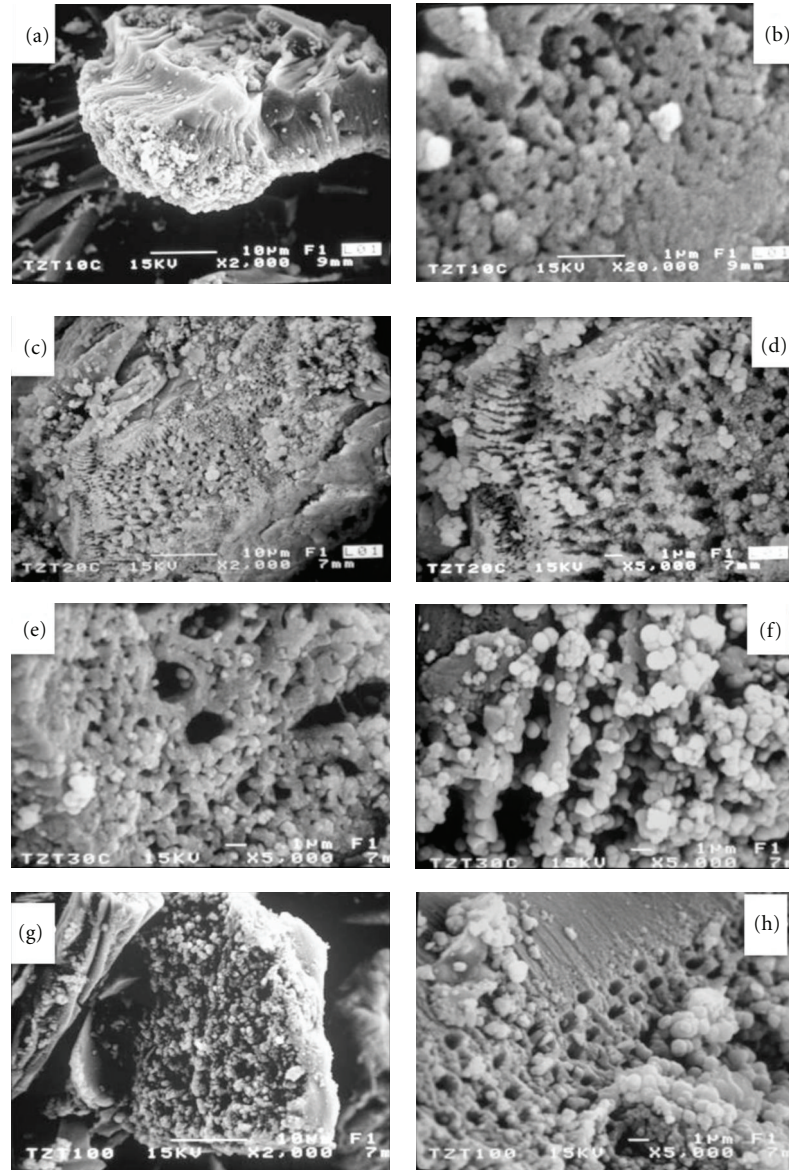


FIGURE 5: SEM micrographs of the T10Z-400 sample ((a) and (b)), T20Z-400 sample ((c) and (d)), T30Z-400 sample ((e) and (f)), and Z-400 sample ((g) and (h)).

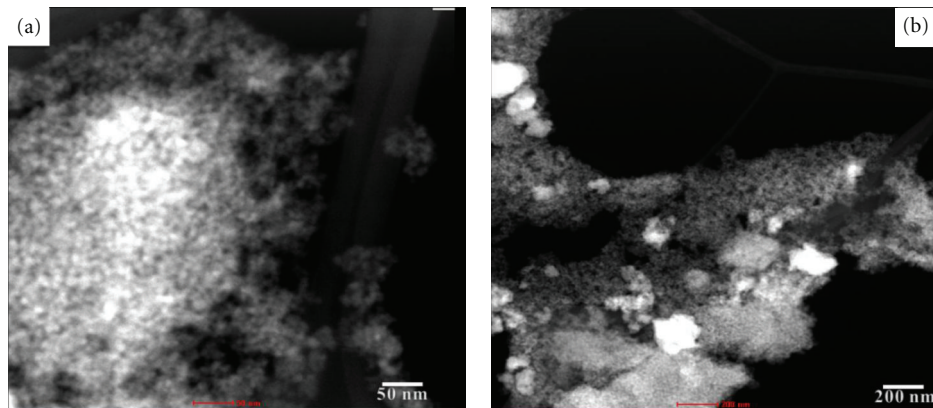


FIGURE 6: TEM image of sample T10Z-400 obtained by Z-contrast technique, (a) macro-mesoporous “sponge-” like agglomerate, (b) different agglomerates, with mesoporous structure.

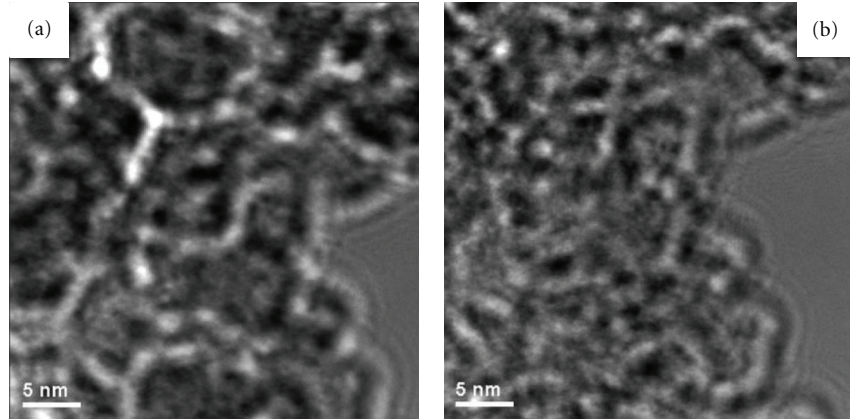


FIGURE 7: TEM image of T20Z-400 sample, presenting the obtained mesoporous with a “worm like structure” (a) underfocus image and (b) overfocus image.

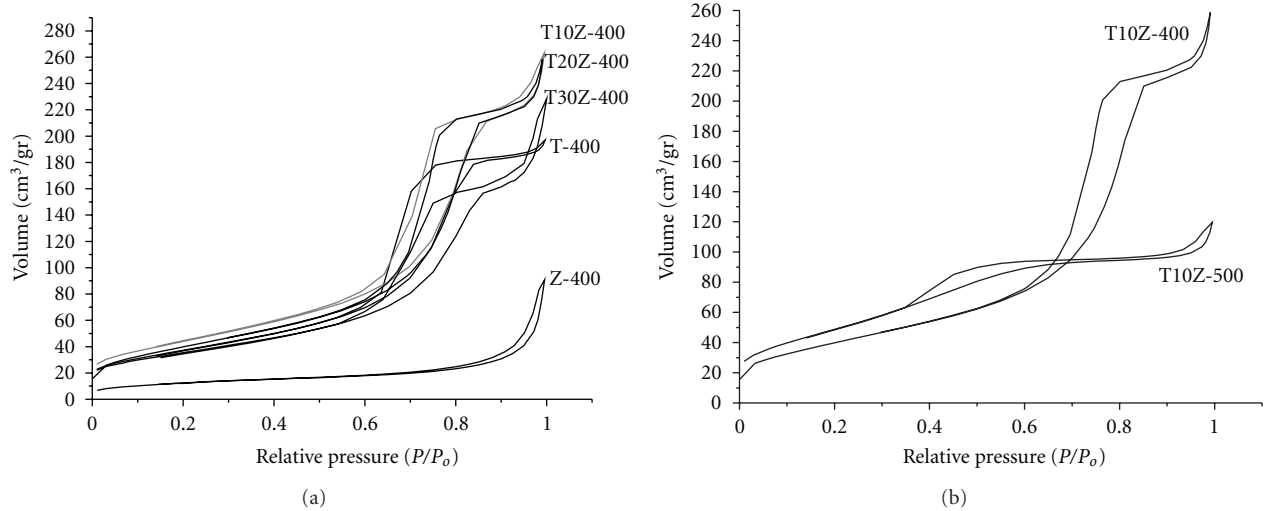


FIGURE 8: Adsorption-desorption N_2 isotherms of the (a) T10Z-400, T20Z-400, T30Z-400, T-400, and Z-400 samples and (b) T10Z-400 and T10Z-500.

was reached for the T10Z-500 sample, which is probably due to the better mesoporous structure formation of this sample leading to the formation of more and smaller mesopores. This explanation can be supported by the N_2 absorption-desorption isotherm corresponding to this sample, shown in Figure 8(b). The isotherm indicates that this sample adsorbs a greater volume of N_2 at lower partial pressure than the other samples and presents two hysteresis loops, one at high and the other at low partial pressures. This isotherm presents the typical form of type IV isotherms, so the calcinations temperature of 500°C in the T10Z-500 sample is really important to lead to a better mesoporous structure formation, and the isotherm suggests that there are also microporosity (pore size $< 2 \text{ nm}$). The mean pore diameter of the T10Z-500 sample is effectively the lowest one, obtained by the BJH method from the corresponding adsorption and desorption data. The obtained specific surface areas are in agreement with those reported by other authors [49, 50].

3.5. Photocatalytic Test. The photocatalytic test with the powders obtained was carried out for the MB degradation. Figure 9 shows the plots of MB degradation versus reaction time; the concentration of MB diminishes with time for all samples. The addition of zirconia provokes a drastic change in the kinetic behavior of the MB degradation reaction, changing it from parabolic for the pure titania sample T-400 and P-25 Degussa powder to lineal for all the mixed samples. The T10Z-400 sample degraded 57% in 4 hours, T20Z-400 and T30Z-400 samples degraded only 18 and 20% respectively, in 4.5 hours; it might be due to the ZrO_2 at high concentrations increases domains of ZrO_2 with band gap = 5 eV resulting in a decrease in the photocatalytic activity because ZrO_2 is difficult to excited even by UV light [51]; additionally, for the ZrO_2 agglomeration increase and the blockout of the porous structure by these agglomerates, see Figure 6(b). The T10Z-500 sample showed the best behavior degrading 90% of the MB initial concentration in 4 hours

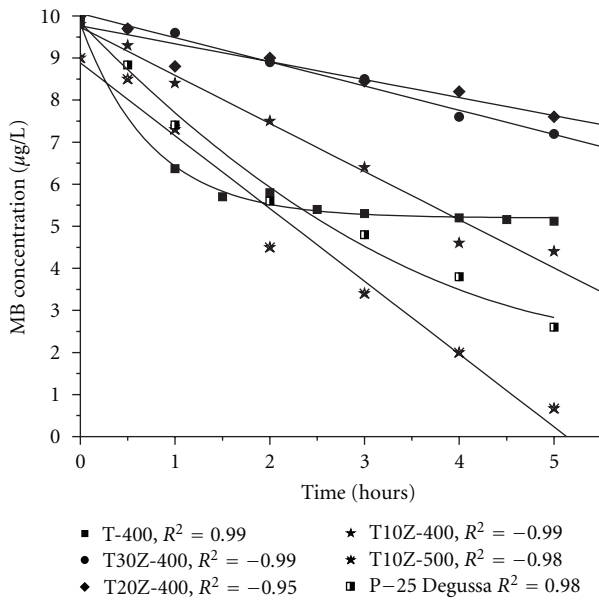


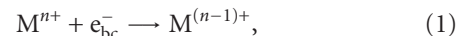
FIGURE 9: Kinetic plots of MB concentration versus reaction time.

and degraded up to 92% at 5 hours of reaction. As a comparison, TiO_2 P-25 Degussa powder presents a parabolic behavior in the degradation of MB curve, as pure titania T-400 sample does, it degraded 66% in 4 hours and degraded up to 70% in 5 hours; this result is accordance with Tayade et al. [52], so it resulted less effective than T10Z-500 sample this result could be due to the smaller crystallite size compared with P-25 Degussa powder [53].

From these results, we conclude that, in order to have better photocatalytic activity, there is an optimal addition of 10% mole of ZrO_2 , due in part to the specific surface area, and the macro-mesoporosity according with Schattka et al. [54] who reported that zirconia additions to titania increased the specific surface areas of titania, they concluded that the presence of zirconia in the titania network, at a molar ratio of 1 : 9, resulted in enhanced photocatalytic activity relative to the pure titania network. A further increase in the ratio of zirconia to titania leads to a decrease in photocatalytic activity, as can be concluded from the photocatalytic test results in the present work. Huang et al. [51] also reported that specific surface areas are increased as the ZrO_2 content is increased but the photocatalytic degradation does not depend on this parameter. They found that $\text{Ti}_{0.91}\text{Zr}_{0.09}\text{O}_2$ solid solution exhibited the highest photocatalytic activity amongst all their samples with S_{BET} area of $67.8 \text{ m}^2/\text{g}$. Otherwise Yu et al. [47] reported better behavior for sample with S_{BET} area of $203 \text{ m}^2/\text{g}$ and crystallite size of 7.1 nm obtained by hydrothermal treatment at 180°C ; this value is similar to S_{BET} T10Z-500, see Table 2.

The way in which zirconia enhances the photocatalytic properties of titania can be explained by band theory, which says that it is possible to create some additional energy states within the band gap which reduces the energy required to liberate an electron and move to the conduction band.

In titania, for example, there are oxygen vacancies that introduce localized Ti^{+3} states which are donor impurities which in turn generate traps near the conduction band, and these traps are not usually recombined [55], in ZrO_2 . Foster et al. [32] found the positions of defect levels with respect to the bottom of silicon conduction band. It is now generally accepted that the addition of transition metals in the structure of titania increases the speed of photooxidation, due to the combination of the electrons to the metal ions in the semiconductor surface according with the following reaction:



where M^{n+} represents transition metals.

This reaction prevents the rapid recombination of those electron-hole pairs generated, resulting in an increase in the rate of formation of OH^- ions on the TiO_2 surface as well as in the reaction solution facilitates the formation of OH^\bullet radicals [26, 52], consequently the efficiency of the process is logically enhanced.

4. Concluding Remarks

A series of TiO_2 - ZrO_2 photocatalytic powder systems with hierarchically macro-mesoporous structures was successfully synthesized by hydrothermal synthesis using Tween-20 as the directing agent, allowing the formation of the bimodal pore size distribution in the mixed oxide system, which remained stable under calcinations up to 500°C . For all the compositions studied, the macropores obtained are in one-dimensional orientation, parallel with each other, and the macroporous framework is composed of interconnected wormhole-like mesopores. The mesoporous sizes of the binary oxides, as well as macropore sizes, could be tailored by the variation of the molar ratios of the metal precursors. The stabilization of the anatase crystalline phase of titania and tetragonal crystalline phase of zirconia was observed in these binary oxides. The role of thermal treatment at 500°C on the improved mesoporous structure formation, on the total elimination of organics and surfactant molecules, and on the resultant photocatalytic activity has been clearly shown. The best photocatalytic behavior was obtained for the sample T10Z-500 with an addition of 10% mole of zirconia, which resulted better than TiO_2 P-25 Degussa powder. These meso-macroporous binary oxides showed higher surface areas as the zirconia content was increased, larger pore volumes and higher thermal stabilities than single metal oxides, exhibited efficient potential for photocatalytic applications.

Acknowledgments

This research was financially supported by CONACYT Project no. 83880 and CIC-UMSNH. The authors gratefully acknowledge Dr. Marco Antonio Medina, Dr. M. Elena Nuñez, and Dr. Ariosto Medina Flores for their technical support.

References

- [1] H. Arora, C. Doty, and Y. Yuan, "Titanium dioxide nanoconjugates," in *Nanomaterials for the Life Sciences*, C. S. S. R. Kumar, Ed., vol. 8, Wiley-VCH, Weinheim, Germany, 2006, Nanoconjugates.
- [2] S. S. Liang, H. Makamba, S. Y. Huang, and S. H. Chen, "Nanotitanium dioxide composites for the enrichment of phosphopeptides," *Journal of Chromatography A*, vol. 1116, no. 1-2, pp. 38–45, 2006.
- [3] C. A. Páez, D. Poelman, J. P. Pirard, and B. Heinrichs, "Unpredictable photocatalytic ability of H₂-reduced rutile-TiO₂ xerogel in the degradation of dye-pollutants under UV and visible light irradiation," *Applied Catalysis B*, vol. 94, no. 3-4, pp. 263–271, 2010.
- [4] W. Ren, Z. Ai, F. Jia, L. Zhang, X. Fan, and Z. Zou, "Low temperature preparation and visible light photocatalytic activity of mesoporous carbon-doped crystalline TiO₂," *Applied Catalysis B*, vol. 69, no. 3-4, pp. 138–144, 2007.
- [5] Q. Xiao, J. Zhang, C. Xiao, Z. Si, and X. Tan, "Solar photocatalytic degradation of methylene blue in carbon-doped TiO₂ nanoparticles suspension," *Solar Energy*, vol. 82, no. 8, pp. 706–713, 2008.
- [6] S. K. Samantaray and K. M. Parida, "Effect of anions on the textural and catalytic activity of titania," *Journal of Materials Science*, vol. 38, no. 9, pp. 1835–1848, 2003.
- [7] R. Asahi, T. Morikawa, T. Ohwaki, K. Aoki, and Y. Taga, "Visible-light photocatalysis in nitrogen-doped titanium oxides," *Science*, vol. 293, no. 5528, pp. 269–271, 2001.
- [8] J. A. Byrne, P. A. Fernandez-Ibañez, P. S. M. Dunlop, D. M. A. Alrousan, and J. W. J. Hamilton, "Photocatalytic enhancement for solar disinfection of water: a review," *International Journal of Photoenergy*, vol. 2011, Article ID 798051, 2011.
- [9] Y. Yao, Y. Ohko, Y. Sekiguchi, A. Fujishima, and Y. Kubota, "Self-sterilization using silicone catheters coated with Ag and TiO₂ nanocomposite thin film," *Journal of Biomedical Materials Research B*, vol. 85, no. 2, pp. 453–460, 2008.
- [10] A. Mo, W. Xu, S. Xian, Y. Li, and S. Bai, "Antibacterial activity of silver-hydroxyapatite/titania nanocomposite coating on titanium against oral bacteria," *Key Engineering Materials*, vol. 330–332, pp. 455–458, 2007, *Bioceramics* 19 (parts 1 and 2).
- [11] G. F. Fu, P. S. Vary, and C. T. Lin, "Anatase TiO₂ nanocomposites for antimicrobial coatings," *Journal of Physical Chemistry B*, vol. 109, no. 18, pp. 8889–8898, 2005.
- [12] L. F. Liu, B. John, K. L. Yeung, and G. Si, "Non-UV based germicidal activity of metal-doped TiO₂ coating on solid surfaces," *Journal of Environmental Sciences*, vol. 19, no. 6, pp. 745–750, 2007.
- [13] B. Mahltig, E. Gutmann, D. C. Meyer et al., "Solvothermal preparation of metalized titania sols for photocatalytic and antimicrobial coatings," *Journal of Materials Chemistry*, vol. 17, no. 22, pp. 2367–2374, 2007.
- [14] D. F. Ollis, "Integrating photocatalysis and membrane technologies for water treatment," *Annals of the New York Academy of Sciences*, vol. 984, pp. 65–84, 2003.
- [15] S. Kohtani, A. Kudo, and T. Sakata, "Spectral sensitization of a TiO₂ semiconductor electrode by CdS microcrystals and its photoelectrochemical properties," *Chemical Physics Letters*, vol. 206, no. 1–4, pp. 166–170, 1993.
- [16] V. Subramanian, Z. Ni, E. G. Seebauer, and R. I. Masel, "Synthesis of high-temperature titania-alumina supports," *Industrial and Engineering Chemistry Research*, vol. 45, no. 11, pp. 3815–3820, 2006.
- [17] M. L. García-Benjume, M. I. Espitia-Cabrera, and M. E. Contreras-García, "Synthesis and characterization of mesoporous nanostructured TiO₂–Al₂O₃ photocatalytic system," in *Processing of Nanoparticle Structures and Composites: Ceramic Transactions*, T. Hinklin and K. Lu, Eds., vol. 208, pp. 79–89, 2009.
- [18] G. Tian, K. Pan, H. Fu, L. Jing, and W. Zhou, "Enhanced photocatalytic activity of S-doped TiO₂–ZrO₂ nanoparticles under visible-light irradiation," *Journal of Hazardous Materials*, vol. 166, no. 2-3, pp. 939–944, 2009.
- [19] J. Y. Zheng, K. Y. Qiu, and Y. Wei, "Investigation of Zr-incorporated mesoporous titania materials via nonsurfactant templated sol-gel route: synthesis, characterization and stability," *Journal of Materials Science*, vol. 38, no. 3, pp. 437–444, 2003.
- [20] F. Fresno, M. D. Hernández-Alonso, D. Tudela, J. M. Coronado, and J. Soria, "Photocatalytic degradation of toluene over doped and coupled (Ti,M)O₂ (M = Sn or Zr) nanocrystalline oxides: influence of the heteroatom distribution on deactivation," *Applied Catalysis B*, vol. 84, no. 3-4, pp. 598–606, 2008.
- [21] C. Wang, A. Geng, Y. Guo, S. Jiang, X. Qu, and L. Li, "A novel preparation of three-dimensionally ordered macroporous M/Ti (M = Zr or Ta) mixed oxide nanoparticles with enhanced photocatalytic activity," *Journal of Colloid and Interface Science*, vol. 301, no. 1, pp. 236–247, 2006.
- [22] M. Xue, L. Huang, J. Q. Wang et al., "The direct synthesis of mesoporous structured MnO₂/TiO₂ nanocomposite: a novel visible-light active photocatalyst with large pore size," *Nanotechnology*, vol. 19, no. 18, Article ID 185604, 2008.
- [23] Q. Wang, D. Yang, D. Chen, Y. Wang, and Z. Jiang, "Synthesis of anatase titania-carbon nanotubes nanocomposites with enhanced photocatalytic activity through a nanocoating-hydrothermal process," *Journal of Nanoparticle Research*, vol. 9, no. 6, pp. 1087–1096, 2007.
- [24] M. L. García-Benjume, M. I. Espitia-Cabrera, and M. E. Contreras-García, "The effect of synthesis parameters on the production of titania nanostructured spherical aggregates," *Journal of Ceramic Processing Research*, vol. 11, no. 2, pp. 198–203, 2010.
- [25] E. Barajas-Ledesma, M. L. García-Benjume, I. Espitia-Cabrera, A. Bravo-Patiño, and M. E. Contreras-García, "Biocide activity of TiO₂ nanostructured films," *Journal of Nano Research*, vol. 9, pp. 17–24, 2010.
- [26] J. Sin, S. Lam, A. R. Mohamed, and K. Lee, "Degrading endocrine disrupting chemicals from wastewater by TiO₂ photocatalysis: a review," *International Journal of Photoenergy*, vol. 2012, Article ID 185159, 2012.
- [27] L. R. Yu, Z. Zhu, K. C. Chan, H. J. Issaq, D. S. Dimitrov, and T. D. Veenstra, "Improved titanium dioxide enrichment of phosphopeptides from HeLa cells and high confident phosphopeptide identification by cross-validation of MS/MS and MS/MS/MS spectra," *Journal of Proteome Research*, vol. 6, no. 11, pp. 4150–4162, 2007.
- [28] K. Ashman and E. L. Villar, "Phosphoproteomics and cancer research," *Clinical & Translational Oncology*, vol. 11, no. 6, pp. 356–362, 2009.
- [29] A. Paradela and J. P. Albar, "Advances in the analysis of protein phosphorylation," *Journal of Proteome Research*, vol. 7, no. 5, pp. 1809–1818, 2008.
- [30] L. Zhang and J. C. Yu, "A sonochemical approach to hierarchical porous titania spheres with enhanced photocatalytic activity," *Chemical Communications*, vol. 9, no. 16, pp. 2078–2079, 2003.

- [31] P. Kluson, H. Luskova, L. Cerveny, J. Klisakova, and T. Cajthaml, "Partial photocatalytic oxidation of cyclopentene over titanium(IV) oxide," *Journal of Molecular Catalysis A*, vol. 242, no. 1-2, pp. 62–67, 2005.
- [32] A. S. Foster, V. B. Sulimov, F. Lopez Gejo, A. L. Shluger, and R. M. Nieminen, "Structure and electrical levels of point defects in monoclinic zirconia," *Physical Review B*, vol. 64, no. 22, Article ID 224108, 10 pages, 2001.
- [33] J. M. Herrmann, "Heterogeneous photocatalysis: state of the art and present applications," *Topics in Catalysis*, vol. 34, no. 1–4, pp. 49–65, 2005.
- [34] J. Yu, L. Zhang, B. Cheng, and Y. Su, "Hydrothermal preparation and photocatalytic activity of hierarchically sponge-like macro-/mesoporous titania," *Journal of Physical Chemistry C*, vol. 111, no. 28, pp. 10582–10589, 2007.
- [35] J. Escobar, J. A. de Los Reyes, and T. Vivéros, "Influence of the synthesis additive on the textural and structural characteristics of sol-gel Al_2O_3 – TiO_2 ," *Industrial and Engineering Chemistry Research*, vol. 39, no. 3, pp. 666–672, 2000.
- [36] E. Muñoz, J. L. Boldú, E. Andrade et al., "Intrinsically formed trivalent titanium ions in sol-gel titania," *Journal of the American Ceramic Society*, vol. 84, no. 2, pp. 392–398, 2001.
- [37] G. Q. Liu, Z. G. Jin, X. X. Liu, T. Wang, and Z. F. Liu, "Anatase TiO_2 porous thin films prepared by sol-gel method using CTAB surfactant," *Journal of Sol-Gel Science and Technology*, vol. 41, no. 1, pp. 49–55, 2007.
- [38] S. G. Liu, H. Wang, J. P. Li, N. Zhao, W. Wei, and Y. H. Sun, "A facile route to synthesize mesoporous zirconia with ultra high thermal stability," *Materials Research Bulletin*, vol. 42, no. 1, pp. 171–176, 2007.
- [39] M. L. García-Benjume, M. I. Espitia-Cabrera, and M. E. Contreras-García, "Hierarchical macro-mesoporous structures in the system TiO_2 – Al_2O_3 , obtained by hydrothermal synthesis using Tween-20 as a directing agent," *Materials Characterization*, vol. 60, no. 12, pp. 1482–1488, 2009.
- [40] F. del Monte, W. Larsen, and J. D. Mackenzie, "Stabilization of tetragonal ZrO_2 in ZrO_2 – SiO_2 binary oxides," *Journal of the American Ceramic Society*, vol. 83, no. 3, pp. 628–634, 2000.
- [41] D. A. Ward and E. I. Ko, "Synthesis and structural transformation of zirconia aerogels," *Chemistry of Materials*, vol. 5, no. 7, pp. 956–969, 1993.
- [42] X. Wang, J. C. Yu, C. Ho, Y. Hou, and X. Fu, "Photocatalytic activity of a hierarchically macro/mesoporous titania," *Langmuir*, vol. 21, no. 6, pp. 2552–2559, 2005.
- [43] U. Ciesla and F. Schüth, "Ordered mesoporous materials," *Microporous and Mesoporous Materials*, vol. 27, no. 2–3, pp. 131–149, 1999.
- [44] X. He and D. Antonelli, "Recent advances in synthesis and applications of transition metal containing mesoporous molecular sieves," *Angewandte Chemie—International Edition*, vol. 41, no. 2, pp. 215–229, 2002.
- [45] J. Yu, Y. Su, and B. Cheng, "Template-free fabrication and enhanced photocatalytic activity of hierarchical macro-/mesoporous titania," *Advanced Functional Materials*, vol. 17, no. 12, pp. 1984–1990, 2007.
- [46] A. Collins, D. Carriazo, S. A. Davis, and S. Mann, "Spontaneous template-free assembly of ordered macroporous titania," *Chemical Communications*, vol. 10, no. 5, pp. 568–569, 2004.
- [47] J. Yu, G. Wang, B. Cheng, and M. Zhou, "Effects of hydrothermal temperature and time on the photocatalytic activity and microstructures of bimodal mesoporous TiO_2 powders," *Applied Catalysis B*, vol. 69, no. 3–4, pp. 171–180, 2007.
- [48] J. Yu, J. C. Yu, W. Ho et al., "Effects of alcohol content and calcination temperature on the textural properties of bimodally mesoporous titania," *Applied Catalysis A*, vol. 255, no. 2, pp. 309–320, 2003.
- [49] C. Flego, L. Carluccio, C. Rizzo, and C. Perego, "Synthesis of mesoporous SiO_2 – ZrO_2 mixed oxides by sol-gel method," *Catalysis Communications*, vol. 2, no. 2, pp. 43–48, 2001.
- [50] J. Zhao, Y. Yue, W. Hua, and Z. Gao, "Catalytic activities and properties of mesoporous sulfated Al_2O_3 – ZrO_2 ," *Catalysis Letters*, vol. 116, no. 1–2, pp. 27–34, 2007.
- [51] Y. Huang, Z. Zheng, Z. Ai, L. Zhang, X. Fan, and Z. Zou, "Core - Shell microspherical $\text{Ti}_{1-x}\text{Zr}_x\text{O}_2$ solid solution photocatalysts directly from ultrasonic spray pyrolysis," *Journal of Physical Chemistry B*, vol. 110, no. 39, pp. 19323–19328, 2006.
- [52] R. J. Tayade, T. S. Natarajan, and H. C. Bajaj, "Photocatalytic degradation of methylene blue dye using ultraviolet light emitting diodes," *Industrial and Engineering Chemistry Research*, vol. 48, no. 23, pp. 10262–10267, 2009.
- [53] Y. Fan, G. Chen, D. Li et al., "Highly selective deethylation of rhodamine B on TiO_2 prepared in supercritical fluids," *International Journal of Photoenergy*, vol. 2012, Article ID 173865, 2012.
- [54] J. H. Schattka, D. G. Shchukin, J. Jia, M. Antonietti, and R. A. Caruso, "Photocatalytic activities of porous titania and titania/zirconia structures formed by using a polymer gel templating technique," *Chemistry of Materials*, vol. 14, no. 12, pp. 5103–5108, 2002.
- [55] A. L. Linsebigler, G. Lu, and J. T. Yates Jr., "Photocatalysis on TiO_2 surfaces: principles, mechanisms, and selected results," *Chemical Reviews*, vol. 95, no. 3, pp. 735–758, 1995.

